Wellbore integrity in a saline aquifer: Experimental steel-cement interface degradation under supercritical CO_2 conditions representative of Brazil's Parana basin

Felipe Dalla Vecchia[a,b,c,*], Victor Hugo Jacks Mendes dos Santos[a,b], Marta Kerber Schütz[a,c], Gabriela Gonçalves Dias Ponzi[a,b], Amanda Sofia de Guimarães e Stepanha[a,b], Célia de Fraga Malfatti[d], Eleani Maria da Costa[b,c]

[a] Pontifical Catholic University of Rio Grande do Sul, PUCRS. Institute of Petroleum and Natural Resources, Avenida Ipiranga, 6681, – TECNOPUC, Building 96J, 90619-900, Porto Alegre, Brazil

[b] Pontifical Catholic University of Rio Grande do Sul, PUCRS, Graduate Program in Materials Engineering and Technology, Avenida Ipiranga, 6681– Building 32, 90619-900, Porto Alegre, Brazil

[c] Pontifical Catholic University of Rio Grande do Sul, PUCRS, School of Technology, Avenida Ipiranga, 6681 – Building 30, 90619-900, Porto Alegre, Brazil

[d] Federal University of Rio Grande do Sul, UFRGS, LAPEC/PPGE3M, Avenida Bento Gonçalves, 9500 Porto Alegre, RS, Brazil

ABSTRACT

From our work, significant progress has been made in understanding the degradation of cement-casing systems. The CO_2 degradation process was evaluated in specimens with a large interfacial defect, such as large annular spaces, voids and/or channels, which may be the result of a poor cementing job. From the experiments showing no interfacial defect, no signs of degradation were observed, while from experiments showing interfacial defect, both the cement and steel undergo significant degradation. In the well casing, the CO_2-rich brine affects the steel phase, leaching Fe^{2+} ions into solution and promoting $FeCO_3$ precipitation on the material surface, while on the cement sheath, two processes are occurring: (i) the portlandite dissolution and (ii) the cement carbonation process. Then, iron (Fe^{2+}) starts to migrate into the cement structure, compromising the material's self-healing and pore-blocking features, while calcium (Ca^{2+}) starts to compose the corrosion film from the formation of mixed carbonates ($Fe_xCa_yCO_3$) so reducing the corrosion layer's protection. Finally, both ions (Ca^{2+} and Fe^{2+}) become so abundant in the material vicinity that they may form calcium carbonate ($CaCO_3$) on the corrosion layer and iron carbonate ($FeCO_3$) in the cement matrix. Thus, from our results, the degradation mechanisms of the cement-casing system in CO_2-rich brine was revised.

1. Introduction

Currently, Carbon Capture and Storage (CCS) is the only viable technology proven to partially mitigate the gaseous emissions from large point sources (Lavrov and Torsæter, 2018; Tiong et al., 2019). Through the implementation of CCS, it is possible to conduct long-term CO_2 geological storage and reduce the impact of global warming. CCS can be considered as a transition technology since it is a method which requires intensive use of materials and energy, however, once it is implemented, a billion tonnes of CO_2 emission per year could be avoided (Metz et al., 2005; Tiong et al., 2019).

In order to ensure the effectiveness of the carbon storage process for hundreds to thousands of years, it is necessary to properly choose the host geological formation (Barlet-Gouédard et al., 2009; Carey et al., 2010). In this context, the Intergovernmental Panel on Climate Change (IPCC) points out that coal seams, depleted oil and gas fields, and deep saline aquifers should be adequate subsurface reservoirs for CCS operations (Koukouzas et al., 2017; Metz et al., 2005). Among them, saline aquifers show the highest storage capacity while at the same time, they are widespread over the world (Laumb et al., 2016; Metz et al., 2005).

As long-term CO_2 storage is the objective of CCS projects (Guthrie et al., 2018), it is possible to point out that fluid leakage is the main perceived risk associated with these projects (Iyer et al., 2018; Onishi et al., 2019). In this context, the wellbore integrity is identified as the most critical issue to the CCS infrastructure since it may provide a

pathway for fluid to escape from the subsurface environment to shallow formations or, in the worst scenario, back to the surface (Bagheri et al., 2018; Li and Nygaard, 2018). Thus, preserving the wellbore integrity throughout the project's operational life cycle (construction, injection, monitoring and abandonment) is a key issue for CCS effectiveness (Omosebi et al., 2017; Postma et al., 2019).

In CCS operations, drilling and completion of wells are crucial steps to access the host reservoir (Ahdaya et al., 2019). The wells are basically composed of a steel casing protected by a cement sheath (Garcia Fernandez et al., 2019; Tremosa et al., 2017). In the completion step, the cementation operations involve the removal of drilling mud and the filling of the annular space between the formation and steel casing with cement paste, to stabilize the well structure and provide the hydraulic seal after cement curing (Omosebi et al., 2016; Wakeel et al., 2019). After reaching the CCS reservoir, the CO_2 storage operation will be conducted by the injection of supercritical CO_2 (scCO_2) through the drilled well (Lesti et al., 2013).

While an effective geological formation-cement-casing bond is responsible for preventing undesirable fluids migration (Kiran et al., 2017; Omosebi et al., 2016), materials applied in well construction (cement and steel casing) may be susceptible to chemical and physical changes over time (Kiran et al., 2017; Tiong et al., 2019). Carbonic acid (H_2CO_3) resulting from CO_2 dissolution in brine is especially aggressive to the wellbore materials, being responsible for deep changes in the cement matrix and causing steel casing corrosion, thus significantly compromising the integrity of the cement-casing interface (Carroll et al., 2016; Celia et al., 2015).

The cement-casing interface is a critical point of the wellbore injection system (Ajayi and Gupta, 2019). Integrity failures such as poor primary cementing and formation of defects such as fractures, microannuli, mud channels and gaps, facilitate the migration of corrosive fluids along the well structure and can result in leakage paths (Carroll et al., 2016; Kiran et al., 2017). In this context, several groups have conducted field surveys to assess the integrity of full-scale wells operating for years or decades in CCS storage site conditions (Carey et al., 2007; Crow et al., 2010; Duguid et al., 2017, 2014).

The full-scale wellbores of SACROC (Carey et al., 2007), CCP2 project (Crow et al., 2010), Weyburn (Hawkes and Gardner, 2013), Cranfield (Duguid et al., 2017, 2014), Ketzin (Gawel et al., 2017) and Mont Terri Rock Laboratory (Manceau et al., 2016) were extensively studied by means of logging techniques and direct wellbore core sampling. Different types of defects (e.g. casing corrosion, microannuli, and cement alteration) can affect the well integrity and have been identified in all full-scale projects (Carey et al., 2007; Crow et al., 2010; Duguid et al., 2017, 2014; Gawel et al., 2017; Manceau et al., 2016). Although none of the authors report a definitive compromise in the integrity of the monitored CCS well, it is known that these defects can lead from a workover operation to a complete stop in the injection process.

Currently, most studies only focus on one of the wellbore system materials (formation-cement-casing) and, although significant work has been done to assess the integrity of the formation-cement interface (Silva and Milestone, 2018a, 2018b), there is a lack of information about the integrity of the cement-casing interface and how the materials interact during the CO_2 degradation process (Jobard et al., 2018; Tremosa et al., 2017). Studies of cement carbonation (Bihua et al., 2018; Koukouzas et al., 2017) and steel casing corrosion (Nešić, 2007) are numerous. However, the evaluation of the cement-casing interface integrity is significantly limited (Asahara et al., 2013; Carey et al., 2010, 2009; Mito et al., 2015; Nakano et al., 2016, 2014; Ren et al., 2016; Wolterbeek et al., 2016, 2013; Wolterbeek and Raoof, 2018). Among them, only three works simulate interface degradation in the presence of wellbore defects (microannuli) and CO_2-rich fluids in dynamic (Carey et al., 2010, 2009) or static (Wolterbeek et al., 2013) systems, considering the simultaneous occurrence of cement carbonation and steel corrosion.

Whereas there is an important lack of data about the cement-casing

degradation dynamics in the presence of a wellbore defect, the present work proposes a study on the cement-casing interface system, with and without an interfacial defect between the wellbore materials. In addition, the interaction of material exchange flows between the cement and casing under a CO_2-rich brine, simulating a saline aquifer storage environment, is inducted and evaluated. Thus, from our study, the degradation dynamics of the cement-casing system in CO_2-rich brine was revised and the importance of the results is discussed in the light of the perspectives of using carbon capture and storage as a technology to partially mitigate greenhouse gas emissions.

2. Materials and methods

The present work evaluates the integrity of the cement-casing interface system under wet degradation conditions by CO_2-rich brine operating at supercritical conditions. Since CCS research has been widely promoted in Brazil, with special emphasis on Petrobras (Iglesias et al., 2015), the experimental setups (brine composition, temperature and pressure) simulate the conditions of the saline aquifer from Paraná-Basin (Brazil). This aquifer has been extensively studied and is pointed out as a potential storage site for CCS projects (Ketzer et al., 2009; Machado et al., 2013).

2.1. Sample preparation

The materials applied to obtain the cement-casing composites are class G cement and the API 5CT N80 steel. The detailed composition of class G cement (Table S1) and of the N80 Steel (Table S2) are presented in the Supplementary Material. The samples (24 specimens) were prepared in order to assess the cement-casing interface degradation dynamics, with (21 specimens) and without (3 specimens) wellbore defect, while a synthetic brine solution was applied to simulate the aquifer environment. Thus, the different scenarios identified in full-scale wells, with and without the presence of an interfacial failure, can be evaluated.

2.1.1. Synthetic aquifer brine

The brine samples from the aquifer (Paraná-Basin) were collected in the municipality of São João do Sul in the state of Santa Catarina. The well was drilled with a depth of approximately 900 m deep by the Mineral Resources Research Company (Companhia de Pesquisa de Recursos Minerais - CPRM), a Brazilian Federal Government Agency. This wellbore accesses the Rio Bonito formation featuring proper porosity, permeability and depth for CO_2 storage (Machado et al., 2013; Rockett et al., 2011). The site location is presented in Fig. S1 in the Supplementary Material. The brine was sampled following the Environmental Protection Agency (U.S. EPA) recommendations and its composition analyzed at Eurofins | Alac laboratory (Garibaldi, RS - Brazil).

After the brine composition determination, a synthetic saline solution was prepared from reagents with analytical grade, simulating the concentrations found in the geological formation environment (saline aquifer from Paraná-Basin, Rio Bonito formation). The experimental procedures used sodium chloride, potassium chloride, calcium sulfate, calcium chloride, strontium chloride, magnesium chloride, and sodium bicarbonate as chemical reagents to prepare the synthetic saline solution and Table 1 presents the compositions of the saline aquifer and synthetic solution brines.

2.1.2. Cement paste

Preparation of the class G cement paste cores was carried out according to American Petroleum Institute - API 10A (2002) with a 0.44 water/cement ratio, no use of additives, and cured under a thermostatic bath (60 °C and atmospheric pressure) for 8 h. A constant speed API mixer (CTE model 7000) was applied to mix cement with water, and subsequently the cement slurry was transferred to PVC molds, as

Table 1
Brine composition of the saline aquifer and respective synthetic solution.

Chemical element	Brine (mg·L^{-1})	Synthetic brine (mg·L^{-1})
Sodium (Na$^+$)	7,866	5,864
Potassium (K$^+$)	125	125
Calcium (Ca^{2+})	2,153	2,066
Magnesium (Mg^{2+})	4	4
Aluminium (Al^{3+})	ND	–
Iron (Fe^{2+} and Fe^{3+})	ND	–
Manganese (Mn^{2+})	0.8	0
Strontium (Sr^{2+})	63	66
Chloride (Cl$^-$)	11,334	11,516
Sulphate (SO$_4^{2-}$)	608	635
Bicarbonate (HCO$_3^-$)	NQ	2,033
Total salinity	22,154	22,309

ND - Not Detected and NQ - Not Quantified.

represented in Fig. S2 of the Supplementary Material. The cement paste specimens are 25 mm in diameter x 50 mm in height. After 8 h of thermal curing the specimens reached an average compression resistance of 33.4 ± 2.8 MPa.

2.1.3. N80 steel bar

The API N80 steel cores were prepared by reducing the dimensions to values of 8 × 8 × 30 mm followed by sanding the surface with sandpaper (220, 320, 400, 600 and 1200 grit) and washing with deionized water. Finally, the steel cores were degreased by immersing the steel samples in acetone for 5 min in an ultrasonic bath. In order to evaluate the steel microstructure by means of optical microscopy, the material surface was treated with Nital alcoholic solution (3% HNO$_3$) and the results are presented in the Supplementary Material, Fig. S3.

2.1.4. Cement-casing specimens

Cement-casing specimens are divided into bonding and no-bonding defect specimens, as represented in Fig. 1. The specimens, showing no interfacial defect (Fig. 1A), were prepared to demonstrate the importance of the cement-casing bond in the presence of aggressive media such as CO$_2$-rich brine at supercritical conditions. Thus, these specimens were made by inserting the steel core at the center of a cylindrical PVC mold, followed by filling of the annular space with cement paste and thermostatic cure.

However, the specimens showing interfacial defect (Fig. 1B and C) were prepared by the insertion of N80 steel bar into a pre-cured class G cement core (25 mm Ø x 50 mm height) with a centralized drilled hole (11 mm Ø x 30 mm deep). The steel bar insertion results in two distinctive interfacial regions, in which *Region 1* presents a perfect cement-casing bonding while *Region 2* presents an interfacial gap of approximately 1.5 mm. Thus, in the present work, the CO$_2$ degradation process was evaluated in specimens with a large interfacial defect, such as large

annular spaces, voids and/or channels, which may be the result of a poor cementing job.

The CO$_2$ degradation of the formation-cement-casing system (materials and interfaces) are usually evaluated in the literature under quasi-static conditions in large pressurized vessels with temperature control (Teodoriu and Bello, 2020). The quasi-static state simulates a condition in which the reaction medium undergoes little mechanical disturbance, with low fluid flows, but which allows material exchange between the cement-casing system through diffusive processes induced by the concentration gradient of chemicals. Thus, it can be considered that assessing the CO$_2$ degradation process in the quasi-static state is appropriate, since many of the cementation defects (e.g. voids, mud channels, small fractures) are not extensive enough to allow considerable fluid flows, and that most of the literature evaluates the integrity of the well materials in a static environment (Bagheri et al., 2018; Teodoriu and Bello, 2020). To simulate the quasi-static condition in the wet carbonation experiments, the top of the cement-casing specimens showing interfacial defect was kept open to allow a material exchange flow with the reactive medium.

2.2. Wet carbonation experiments

The quasi-static environment is reported as the most appropriate model to simulate the well condition dynamics in a CCS storage site (Bagheri et al., 2018), since no continuous fluid channels seem to be widespread in these geological formations (Lavrov, 2018). Thus, the wet degradation experiments in the presence of CO$_2$-rich brine were carried out under quasi-static conditions and CO$_2$ in the supercritical state (15 MPa and 70 °C).

The standardized exposure times were 48–360–720 h and the reaction medium was previously de-aerated by purging with nitrogen gas. In all the wet carbonation degradation experiments, the cement-casing specimens had the same age at the beginning of the procedure. The reaction system representation is shown in Fig. S4 in the Supplementary Material.

2.3. Sample characterization

Cement paste, steel and brine samples were characterized by optical microscopy, scanning electron microscopy with energy dispersive spectroscopy (SEM-EDS), inductively coupled plasma optical emission spectrometry (ICP-OES) and electrochemical analysis, as briefly described below.

2.3.1. Surface and degradation/corrosion products analysis

From microscopic analysis, information was obtained about the surface morphologies of the initial materials, cement paste degradation products, and the corrosion product layers formed on the steel. Cement,
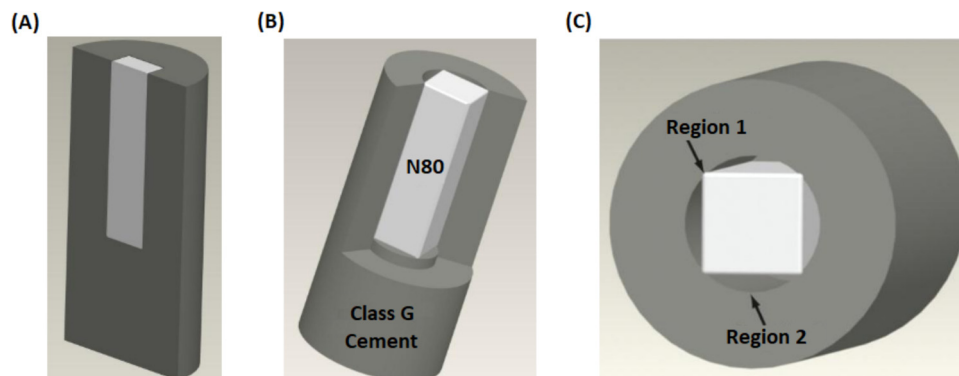

Fig. 1. Cement-casing specimen applied for wet degradation experiments in CO$_2$-rich brine: (A) cement-casing specimen showing no interfacial defect (B) perspective view of the cement-casing specimen showing interfacial defect and (C) front view of the cement-casing specimen showing interfacial defect.
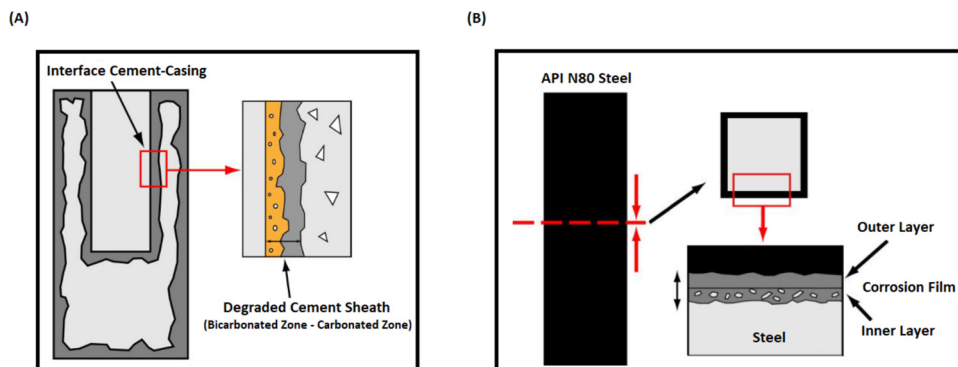
Fig. 2. Scheme of degraded layer evaluation at the cement-casing interfaces: (A) cement paste carbonation and (B) N80 steel corrosion layer.

steel and cement-casing specimens optical microscopic analysis used a PMG3 (Olympus) microscope, while SEM-EDS analysis used XL 30 (Philips) equipment. In the present work, EDS analyses were performed in area and line scan mode. SEM-EDS line scan analysis allows the estimation of the elemental mass fraction of calcium (Ca), silicon (Si), carbon (C), iron (Fe) and oxygen (O) in the cement and steel phases. These analyses are useful to evaluate the material exchange flow in the cement-casing carbonation process giving support to the discussion about wellbore material degradation process dynamics in the presence of interfacial defect.

2.3.2. Degraded layer analysis

The determination of cement and steel degraded layer thicknesses was carried out based on optical and SEM microscopy images using ImageJ® image processing and analysis software. For each specimen, at least 40 measurements were performed to obtain the average results of their degraded layer thickness. The scheme of the degraded layer evaluation is presented in Fig. 2.

Cement degraded layer thicknesses (composed of carbonated and bicarbonated zones) were measured from the longitudinal section of the cement cores after removing the steel bar, as shown in Fig. 2A. Corrosion layer thickness measurements were performed using SEM images of N80 steel cross sections, as shown in Fig. 2B. In addition, the total thickness of the corrosion film, the inner and outer layers of the corrosion scale, are exemplified in the Supplementary Material Fig. S5.

2.3.3. Synthetic brine analysis

Ca^{2+} and Fe^{2+} analysis of the initial (before carbonation) and final (after carbonation) brine solution were determined by inductively coupled plasma optical emission spectrometry (ICP-OES) in an outsourced laboratory.

2.3.4. Steel electrochemical analysis

After the wet degradation experiments, steel cores from the specimens showing interfacial defect were removed, washed with deionized water and stored in a vacuum desiccator. The potentiodynamic polarization tests were performed on model 273A potentiostat/galvanostat (EG&G Princeton Applied Research) to evaluate the influence of the degraded layer on the material corrosion resistance. Measurements were performed at room temperature in a standardized medium (naturally aerated and static conditions) with a 0.05 M NaCl electrolyte. For comparison purposes, a reference sample (polished and non-degraded API N80 steel core) was analyzed in the same way. Potentiodynamic polarization analyzes were performed immediately after the completion of the CO_2 degradation tests and sample preparation.

Before the polarization test, open-circuit potential (OCP) was monitored during the first hour to observe the stability behavior of the corrosion layer formed on the steel surface. Then, polarization curves were obtained with a scan rate of 1 mV per second, from -200 mV to $+300$ mV, with respect to OCP. Finally, potentiodynamic polarization data were treated using CorrView ™ software to obtain the corrosion potential (Ecorr - mV), the corrosion current density (icorr - μA/cm²), the polarization resistance (PR - Ωcm²) and the corrosion rates (CR - mm/year), following ASTM G3-14 (ASTM International, 2019) and ASTM-G102 (ASTM International, 2015).

2.3.5. Thermogravimetric analyzes

The thermogravimetric analysis (TGA) was used to identify the presence of calcium carbonates in the solid precipitates formed after the CO_2 degradation experiments. The precipitate was previously dried, and the analysis was performed on the SDT Q-600 of the TA instruments.
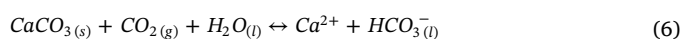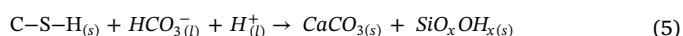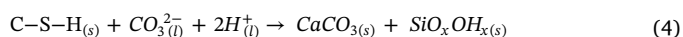
2.4. Cement-casing reactions

There is a consensus based on field and laboratory data that both cement and steel materials are susceptible to changes in CO_2-rich media in CCS sites (Bai et al., 2015b). Additionally, it is pointed out that wellbore interfaces (geological formation-cement-casing) are fragile points of the isolation systems (Kiran et al., 2017; Lorek et al., 2016). Thus, the cement-casing system presenting interfacial defect can be represented as a quasi-static system with a dynamic flux of material between the cement, steel and CO_2-rich brine phases. Thus, it is important to represent the most important reactions involved throughout the wet carbonation process.

The wet carbonation process starts from CO_2 dissolution in water, with the consequent production of $H_2CO_{3(l)}$, $HCO_{3(l)}^-$ and /or $CO_{3(l)}^{2-}$, depending on the medium's pH (Bai et al., 2015a; Duguid et al., 2011). These reactions are represented by Eq. 1.

$$CO_{2(g)} + H_2O_{(l)} \leftrightarrow H_2CO_{3(l)} \leftrightarrow HCO_{3(l)}^- + H_{(l)}^+ \leftrightarrow CO_{3(l)}^{2-} + 2H_{(l)}^+ \qquad (1)$$
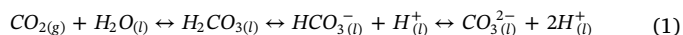
2.4.1. Cement paste carbonation

Cement paste carbonation processes are widely known and the main reactions lead to the degradation of the $Ca(OH)_2$ or portlandite (CH) and calcium silicate hydrate (C-S-H) phases, to produce different calcium carbonate ($CaCO_3$) polymorphs such as calcite, aragonite and vaterite (Duguid et al., 2011; Koukouzas et al., 2017). These reactions are represented by Eqs. 2–7.
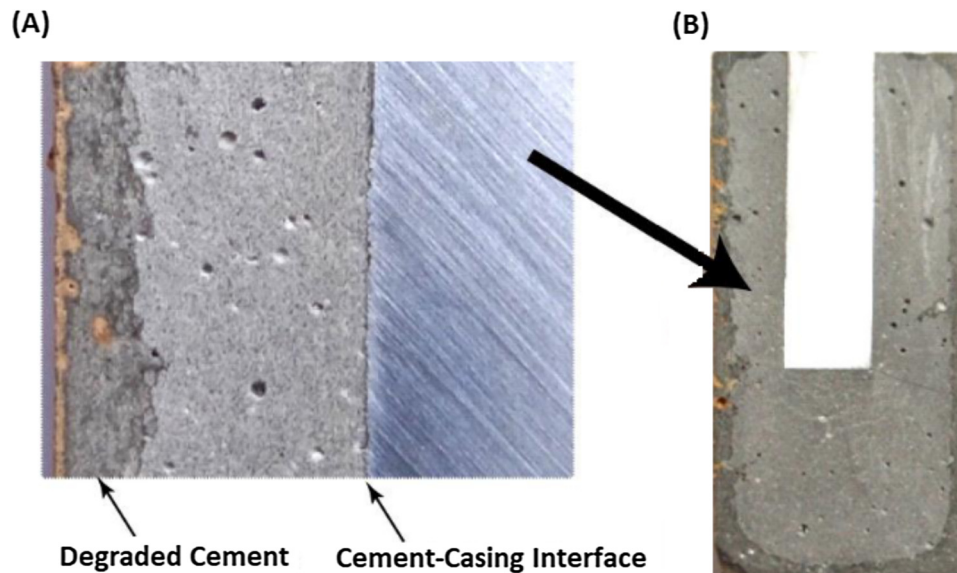
$$Ca(OH)_{2(s)} + CO_{3(l)}^{2-} + 2H_{(l)}^+ \rightarrow CaCO_{3(s)} + 2H_2O_{(l)} \qquad (2)$$

$$Ca(OH)_{2(s)} + HCO_{3(l)}^- + H_{(l)}^+ \rightarrow CaCO_{3(s)} + 2H_2O_{(l)} \qquad (3)$$

$$C{-}S{-}H_{(s)} + CO_{3(l)}^{2-} + 2H_{(l)}^+ \rightarrow CaCO_{3(s)} + SiO_xOH_{x(s)} \qquad (4)$$

$$C{-}S{-}H_{(s)} + HCO_{3(l)}^- + H_{(l)}^+ \rightarrow CaCO_{3(s)} + SiO_xOH_{x(s)} \qquad (5)$$

$$CaCO_{3(s)} + CO_{2(g)} + H_2O_{(l)} \leftrightarrow Ca^{2+} + HCO_{3(l)}^- \qquad (6)$$
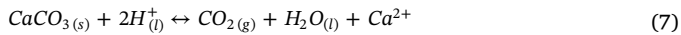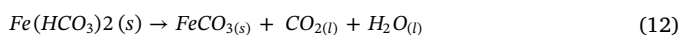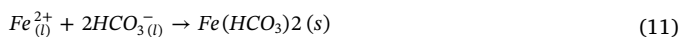
Fig. 3. Cement-casing interfaces of the sample showing no interfacial defect: (A) degraded cement layer and (B) Interface presenting no signs of steel corrosion.

$$CaCO_{3(s)} + 2H^+_{(l)} \leftrightarrow CO_{2(g)} + H_2O_{(l)} + Ca^{2+} \tag{7}$$

2.4.2. Steel casing corrosion

Steel corrosion in CO_2-rich environments has also been well documented in the literature with corrosion rates reaching 20 mm/year (Choi et al., 2013). Corrosion can occur in different ways, which are homogeneous corrosion which must have a maximum rate of 0.1 mm/year, or concentrated (pitting corrosion) that should be avoided (Pfennig et al., 2017, 2013). Thus, the cement-casing bonding quality is a fundamental aspect of the wellbore integrity, since the cement acts as a protective element of the casing surface (Bai et al., 2015a; Pfennig et al., 2013).

The corrosion process in CO_2-rich environments forms a siderite ($FeCO_3$) layer on the steel surface as the main corrosion product, but other materials may also be present, according to Eqs. 8–12 (Carey et al., 2010; Nešić, 2007; Pfennig et al., 2017). The siderite layer shows protective features which may reduce the corrosion rate and prevent significant losses of wellbore the casing integrity (Pfennig and Kranzmann, 2018).

$$Fe_{(s)} \rightarrow Fe^{2+}_{(l)} + 2e^- \tag{8}$$

$$Fe^{2+}_{(l)} + CO_3^{2-}_{(l)} \rightarrow FeCO_{3(s)} \tag{9}$$

$$H^+_{(l)} + 2e^- \rightarrow H_{2(g)} \tag{10}$$

$$Fe^{2+}_{(l)} + 2HCO_3^-_{(l)} \rightarrow Fe(HCO_3)2_{(s)} \tag{11}$$

$$Fe(HCO_3)2_{(s)} \rightarrow FeCO_{3(s)} + CO_{2(l)} + H_2O_{(l)} \tag{12}$$

2.4.3. Cement-casing interface

Most studies focus only on one of the wellbore system materials (cement or casing or formation). Thus, there is lack of information on how these systems interact throughout the degradation process (Jobard et al., 2018; Tremosa et al., 2017). Thus, the mass flow exchange between the cement and casing materials, and the reactions of the cement-casing system have been insufficiently studied by the researchers and are poorly reported in the literature. Thus, in addition to the previously detailed reactions, this dynamic process results in the formation of mixed iron and calcium carbonates in both phases (cement and steel), as represented by Eq. 13.

$$xFe^{2+}_{(l)} + yCa^{2+}_{(l)} + CO_3^{2-}_{(l)} \rightarrow Fe_xCa_yCO_{3(s)} \tag{13}$$
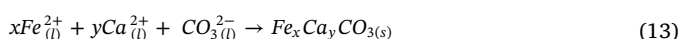
The presence of mixed carbonates ($Fe_xCa_yCO_3$, where x + y = 1) has already been identified at the cement-casing interface. However, only a few reports are found in literature (Carey et al., 2010; Wolterbeek et al., 2013). These degradation products range from almost pure $FeCO_3$ to almost pure $CaCO_3$ as iron (Fe^{2+}) and calcium (Ca^{2+}) concentrations evolve with time and medium mineral saturation (Carey et al., 2010; Ding et al., 2009; Navabzadeh Esmaeely et al., 2013). Mixed carbonate formation may change the corrosion layer protective nature and the self-healing cement ability (Navabzadeh Esmaeely et al., 2013; Wolterbeek et al., 2013).

2.5. Data analysis

Univariate statistical methods are sometimes inefficient in complex system evaluations such as cement-casing interface systems. Thus, considering the amount of experimental data, Correlation Analysis (CA) and Principal Component Analysis (PCA) were performed using the Solo + MIA software (Eigenvector Research) to perform data analysis in order to improve our understanding of the CO_2 degradation process of the cement-casing system. PCA is an exploratory analysis tool applied to put together large datasets in a small dimensional space. The data structure is represented by uncorrelated variables, orthogonally plotted against each other, called principal components (PCs) (Rocha et al., 2012; Vasanthavigar et al., 2013). Through this approach, the most valuable information (explained variance) is extracted and represented by the Score (sample projection) and Loading (variable influence) graphics. Since the data are presented in different units, it was necessary to perform the data scaling followed by the mean centering process to assign similar weights to each of the variables in the PCA.

3. Results and discussion

3.1. Cement-casing system: showing no interfacial defect

Wet carbonation of cement-casing specimens showing no interfacial defect were evaluated firstly. These experiments simulate a condition in which well drilling, and completion processes result in a perfect bonding between the cement and casing along the wellbore. Such carbonation experiments were performed for 168 h, 15 MPa and 70 °C, and the results are presented in Fig. 3.

From optical microscopy analysis, no signs of degradation or fluid intrusion were observed along the cement-casing interface, with the

outer layer degradation of the cement only being noticeable. For these specimens, cement and steel integrity in the interface were preserved, meaning that the wellbore integrity is assured. Similar results were found from field (Carey et al., 2007; Duguid et al., 2014) and laboratory scale experiments (Mito et al., 2015; Nakano et al., 2016; Ren et al., 2016) indicating that perfectly bonded cement-casing interfaces may efficiently protect the casing against CO_2 induced degradation and act as a barrier to prevent CO_2 leakage from the geological formation (Beck et al., 2016; Carroll et al., 2016).

However, other studies indicate that the cement-casing interface may lose its integrity over time in aggressive environments (Lorek et al., 2016; Ren et al., 2016) whereas field data show that interfacial defects are present to some extent of all wells evaluated (Carey et al., 2007; Duguid et al., 2014; Hawkes and Gardner, 2013). Thus, since interfacial defects between the cement and casing are frequent, it is necessary to study these systems in the presence of corrosive fluids and an interfacial gap between these materials and to consider the mass exchange between the cement and casing phases as well.

3.2. Cement-casing system: showing interfacial defect

The interfacial gap used in the specimens (approximately 1.5 mm) is larger than those previously evaluated in different experimental works showing interfacial gaps of the order of a few micrometers (Carey et al., 2010, 2009; Wolterbeek et al., 2013). Since the system is evaluated in a quasi-static environment, both phases (cement and steel) can significantly influence the pH and ions concentration between the interfacial spaces. Fig. 4 illustrates the result of the wet degradation for a sample showing interfacial defect in CO_2-rich brine after 720 h of exposure.

After the steel core removal from specimens, samples were evaluated by means of optical and SEM microscopy. After removing the steel core, the longitudinal sections of cement paste cylinders which underwent 48 h, 360 h and 720 h of exposure to CO_2-rich brine, are shown in Fig. S6 of the Supplementary Material. CO_2-rich brine medium promotes generalized changes in the cement paste and steel core, from a dark-colored layer in the cement to a black scale on the steel core surface. Regarding *Region 2* (Fig. 4), which represents the area showing interfacial defect, signs of deep changes in the cement phase and the presence of $CaCO_3$ precipitated on the cement surface can be seen. The presence of calcium carbonate was confirmed by means of thermogravimetric analysis (Fig. S7). In Fig. 4C, chemically altered layer features, constituted by carbonated and bicarbonated zones, are observed. Also, as observed in experiments showing no interfacial defect, *Region 1* showed no significant signs of degradation (Fig. 4A and B), reinforcing once again the mutual protective aspects related to cement and steel casing.

In addition, the results indicate signs of material exchange between the cement, brine and steel phases, from reddish-colored areas observed on the cement surface, white precipitates on the steel surface and changes in concentration of calcium (Ca^{2+}) and iron (Fe^{2+}) ions in the solution (Fig. S8 in the Supplementary Material). The reddish

precipitates were previously attributed to the presence of iron in the medium (Carey et al., 2007; Wolterbeek et al., 2013), whereas the presence of white crystals on the steel surface indicates the formation of $CaCO_3$ on the corrosion layer (Navabzadeh Esmaeely et al., 2013). From the ICP-OES results (Fig. S8) we may observe a progressive reduction of Ca^{2+} concentration in solution, suggesting the occurrence of precipitation in the form of carbonates. Otherwise, iron (Fe^{2+}) concentration in brine solution indicates that an initial period of steel dissolution and a consequent increase of Fe^{2+} is followed by ion reduction caused by precipitation.

3.2.1. Degraded layer evaluation

The material resistance over time presents great importance for the CCS wellbore integrity. Thus, the exposure time influence in both the cement degradation evolution and steel corrosion layer were evaluated by means of SEM (Fig. 5).

From SEM images, the results show that chemically altered layer increases over time for both materials (cement and steel). The average altered cement layer depths (carbonated zone + bicarbonated zone) at different exposure times are 0.35 mm (48 h), 0.89 mm (360 h) and 0.91 mm (720 h), whereas the total corroded layer (outer layer + inner layer) are 24.60 μm (48 h), 26.19 μm (360 h) and 31.42 μm (720 h). Table 2 details information about the layer thicknesses of the degraded cement and corroded steel.

Regarding the cement paste, initially the carbonation front advances significantly into the cement matrix (Fig. 5A and B). As CO_2-rich brine percolates through the porous cement structure, $CaCO_3$ formation from the consumption of portlandite and C-S-H is observed (Duguid et al., 2011; Koukouzas et al., 2017). These reactions (Eqs. 2–5) show the effect of reducing cement porosity since $CaCO_3$ acts as an expansive pore blocking agent (Fig. 5B) and starts to fill the voids (Bagheri et al., 2018; Tiong et al., 2019). Thus, the reduction of porosity prevents further advances in the cement degradation front. Finally, once the Ca (OH)$_2$ content is depleted, pore fluid pH reduces, favoring the formation of bicarbonate ions and allowing carbonate dissolution (Eq. 6 and 7), thus resulting in a highly porous bicarbonated zone (Fig. 5C) (Barlet-Gouédard et al., 2007; Bjørge et al., 2019). The bicarbonation reaction is considered the most critical reaction for the cement paste integrity since this highly porous layer allows the flow of CO_2-rich brine along the interface and exposes the steel casing to corrosive fluids (Bjørge et al., 2019; Duguid and Scherer, 2010).

Fig. 5D–F show SEM images of steel core cross sections after degradation experiments for 48 h, 360 h and 720 h, respectively. In the present study, only homogeneous corrosion was observed without signs of pitting corrosion. From the images we may obtain the corrosion layer thicknesses as well as observe its morphological features. Similarly, casing corrosion presents a higher initial rate, reducing with the CO_2-rich brine exposure time. Corrosion rate reduction is usually attributed to the formation of a protective layer composed mainly of iron carbonate ($FeCO_3$). This may reduce the corrosion rates from around 20 mm/year to less than 0.1 mm/year (Navabzadeh Esmaeely et al., 2013; Pfennig et al., 2013). A number of corrosion rates are described in the
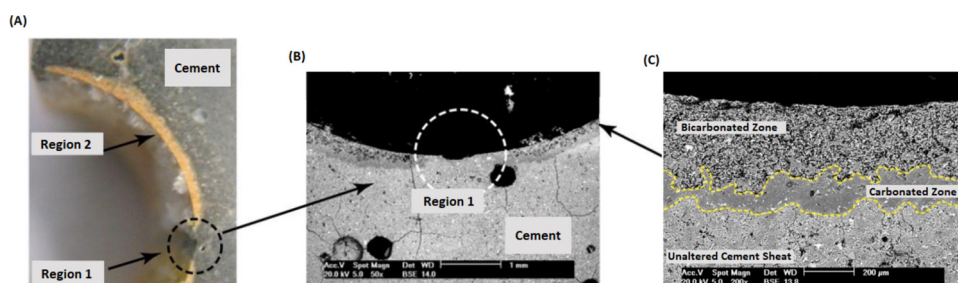

Fig. 4. Cement-casing interfaces of the sample showing interfacial defect: (A) Front view of the cement core, (B) cement-casing interface cross-section SEM image and (C) cement degraded layer cross-section SEM image.
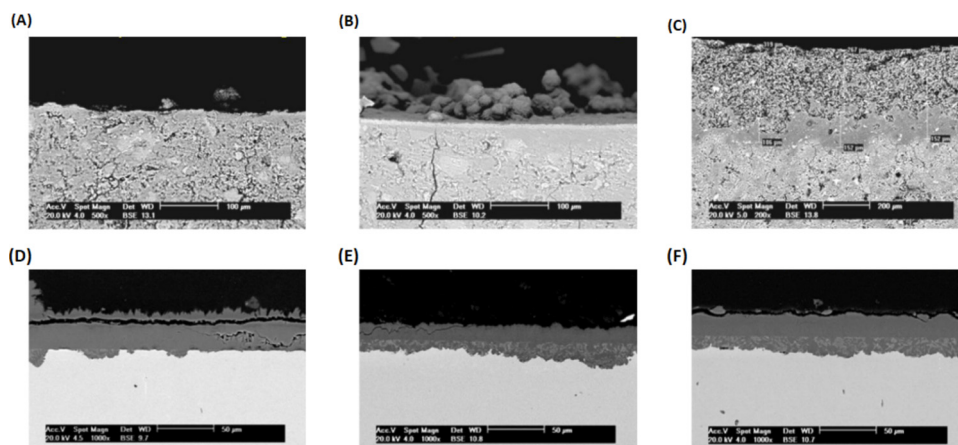
Fig. 5. Evolution of the corrosion and degraded layers at the cement-casing interface at different exposure times. Cement after (A) 48 h, (B) 360 h, and (C) 720 h; steel core after (D) 48 h, (E) 360 h and (F) 720 h.

Table 2
Degradation layer results of the cement-casing interface materials.

Material	Parameters	Time			
		0 h	48 h	360 h	720 h
Cement	Total carbonated layer (mm)	0.000	0.3571	0.8993	0.9113
	Bicarbonated layer (µm)	0.00	0.10	0.10	285.19
Steel	Outer layer (µm)	0	21.95	14.56	17.65
	Inner layer (µm)	0	2.65	11.63	13.77
	Total corroded layer (µm)	0	24.60	26.19	31.42

literature since protective characteristics of the corrosion film present direct relationships with texture, porosity and compaction of the deposited layer on the steel surface (Choi et al., 2013; Navabzadeh Esmaeely et al., 2013).

Regarding steel cores, we may observe the corrosion layer divided into two layers. In the present work, only the corrosion layers (inner or outer) were measured and eventual changes in the total dimensions of the steel cores due to the presence of precipitates or the dissolution of the corrosion products were not evaluated. The outer layer is composed of external corrosion products deposited over the steel surface whereas the inner layer comprises the corrosion front advancing towards the center of the steel core. From SEM images we may see that the outer layer shows more uniform textures than the inner layer. Moreover, the outer/inner thickness layer ratio presents higher values in short exposure time experiments, whereas this layer ratio reduces in longer time experiments. Nešić (2007) observed the same behavior and stated that the system can continue to suffer corrosion even with the presence of corrosion product films. In addition, the outer/inner layer thickness oscillation indicates the existence of corrosion film dissolution and re-precipitation processes.

3.2.2. Degradation/corrosion products at cement-casing interface

Morphology and porosity in wellbore materials play key roles in cement and steel bonding (Silva and Milestone, 2018b). Both properties can be altered as the degradation in CO_2-rich brine progresses, definitely compromising the cement-casing cohesion and wellbore integrity (Bagheri et al., 2018; Koukouzas et al., 2017). Fig. 6 presents SEM images from cement paste (Fig. 6A, C and E) and steel surface (Fig. 6B, D and F) obtained in the interface defect region for each exposure time evaluated.

From Figures (6A to 6 F) we may observe that cement and steel surfaces in the interfacial region change with time. Precipitate morphologies observed in the cement surface at shorter times (48 h - Fig. 6A) present crystalline structures related to $CaCO_3$ polymorphs.

Otherwise, the precipitates obtained at longer exposure times (Fig. 6C and E) present amorphous features, showing signs of mineral dissolution from the cement surface. From Figs. (6 B, D and F), we may observe that in the first 48 h of reaction (Fig. 6B) the corrosion layer formed on the steel surface irregularly covers the casing material. However, precipitates obtained at longer exposure times (Fig. 6D and F) present porous and less compacted features, meaning that these corrosion products may be less protective than those formed at a shorter time. In addition, precipitates observed in the cement at shorter times (Fig. 6A), and steel submitted to 720 h (Fig. 6F) of wet degradation, have similar morphologies, indicating the formation of polymorphic $CaCO_3$ on the steel surface.

Aiming to identify the elemental precipitate composition on the cement and steel surfaces in the interface defect region, EDS analysis was performed on the sample surfaces shown on the SEM images in Fig. 6. The material surface elemental composition is detailed in Table 3, and a graphical representation is presented in the Supplementary Material (Fig. S9).

EDS results (acquired by area) show the elemental precipitate profiles in the degraded material surface (cement and steel) at different exposure times in CO_2-rich brine. According to Table 3, both iron (Fe) and calcium (Ca) are identified on the surface of cement and steel materials at all degradation exposure times. In addition, a tendency of Ca reduction and Fe increase is observed on the cement surface as exposure times increase. Conversely, as exposure times increase, the precipitate profiles on the steel surface change from Fe-rich to Ca-rich materials. Thus, elemental composition suggests the formation of mixed iron and calcium carbonates ($Fe_xCa_yCO_3$) on the surface of both materials indicating material exchange flows among the cement, steel and CO_2-rich brine. These mixed carbonates have been previously identified as composing the precipitate fraction on cement and steel exposed to CO_2, Ca^{2+} and Fe^{2+} rich media (Alsaiari et al., 2008; Carey et al., 2010; Navabzadeh Esmaeely et al., 2013). Even considering that EDS analysis is a semi-quantitative method, variations in the elemental composition on the cement-casing system along the exposure time to the CO_2-rich brine were identified.

3.2.3. Electrochemical analysis of steel

After evaluating the corrosion film morphology and chemical composition, open-circuit potential (OCP) analysis and potentiodynamic polarization measurements were applied in order to evaluate the protectiveness of the corrosion layer (Fig. 7). The electrochemical behavior can be correlated with the corrosion film's properties such as permeability, covering regularity, thickness and protective effectiveness.

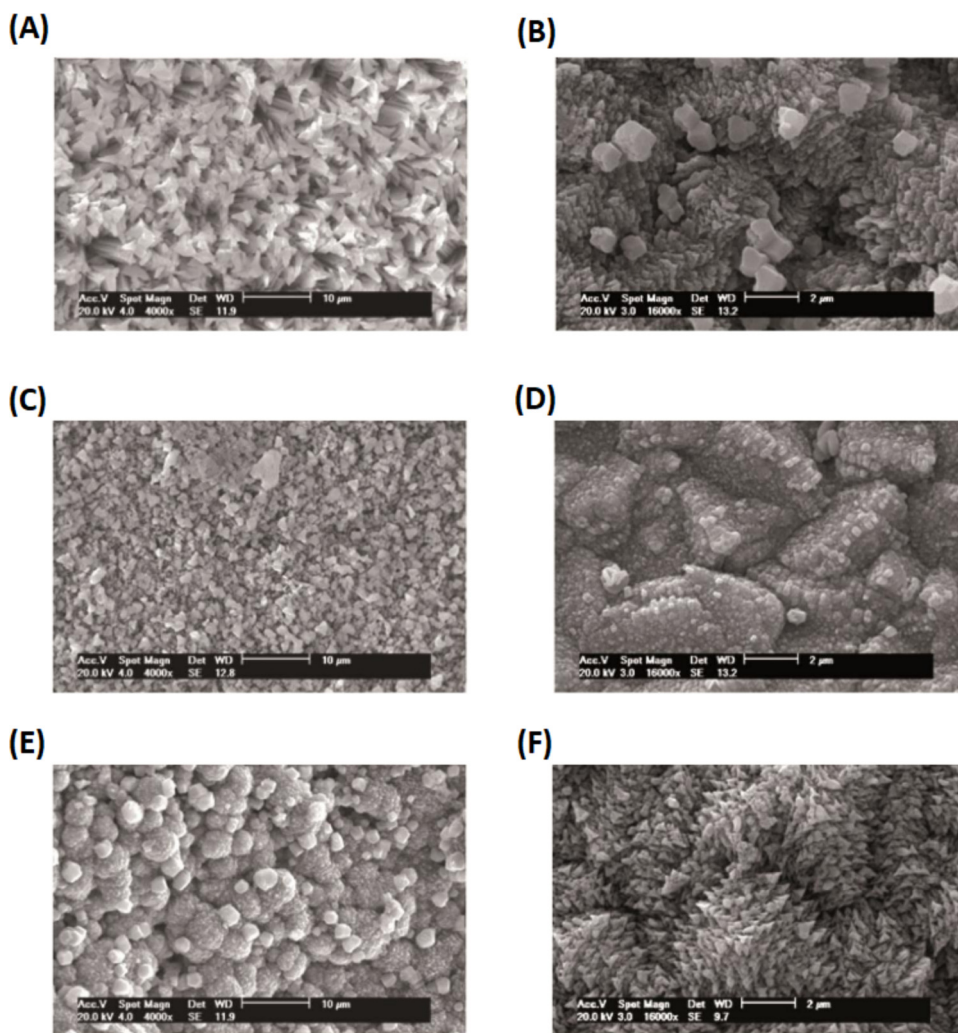After all wet carbonation experiments, the steel bar was removed

Fig. 6. Degraded layer morphology of the cement-casing interface at different CO_2-rich brine exposure times: cement after (A) 48 h, (C) 360 h and (E) 720 h; and steel after (B) 48 h, (D) 360 h and (F) 720 h.

Table 3
EDS elemental results of the cement-casing interface materials.

Material	Parameters	Time			
		0 h	48 h	360 h	720 h
Cement	C-Fe (%)	–	6.09	32.72	29.23
	C-C (%)	–	1.67	2.31	1.64
	C-O (%)	–	39.77	28.96	37.72
	C-Ca (%)	–	52.47	36.01	31.3
Steel	S-Fe (%)	–	44.32	54.51	32.09
	S-C (%)	–	1.17	1.31	2.16
	S-O (%)	–	26.49	22.66	31.19
	S-Ca (%)	–	26.28	19.37	34.55

C - cement phase and S - steel phase.

from the cement cylinders and left immersed for 1 h in 0.05 M NaCl solution. From Fig. 7A, we may observe that all corrosion films formed on the steel surface shift the OCP to more positive values when compared to the reference, showing the following decreasing order in OCP values: 360 h > 48 h > 720 h > Reference. This feature indicates that the corrosion product protection efficiency improves at first (0 h–360 h). In contrast, for long exposure times (720 h), the corrosion film presents no adequate stability and begins to lose its casing protection efficiency against corrosion. In general, the OCP results point out that all steel cores exposed to the CO_2-rich brine show less active

OCP than those obtained by the reference.

The results of potentiodynamic polarization tests (Fig. 7B) show corrosion potentials in the following increasing order: 360 h < 48 h < 720 h < Reference. These results confirm the previous observation that, after an initial metal surface passivation period (0 h–360 h), an inversion in the corrosion film protection tendency takes place for specimens exposed to CO_2-rich brine at longer exposures times. The results of corrosion potential (Ecorr), corrosion current (icorr), polarization resistance (PR) and corrosion rate (CR), obtained from potentiodynamic polarization data, are presented in Table 4.

Results of corrosion potential, corrosion current density, polarization resistance and corrosion rate are related to one another, confirming the statements about the corrosion film morphology and its influence over the corrosion rates obtained for the samples at different exposure times: Reference (0.1081 mm/year) > 720 h (0.0037 mm/year) > 48 h (0.0003 mm/year) > 360 h (0.0001 mm/year). From the electrochemical results, we can assume that the inner and outer corrosion layer growth and dissolution cycles may be affecting the film's ability to protect the steel from further corrosion. Thus, there is a need to evaluate the cement-casing interface system looking at the dynamics between the material phases (cement and steel) and the medium (CO_2-rich brine) as well as material exchange flows along the exposure time. However, as a consequence, assessment of the dissolution cycles of the corrosion products on the corrosion rates, resulting from the outer / inner layer thickness oscillation, must be evaluated and modeled in
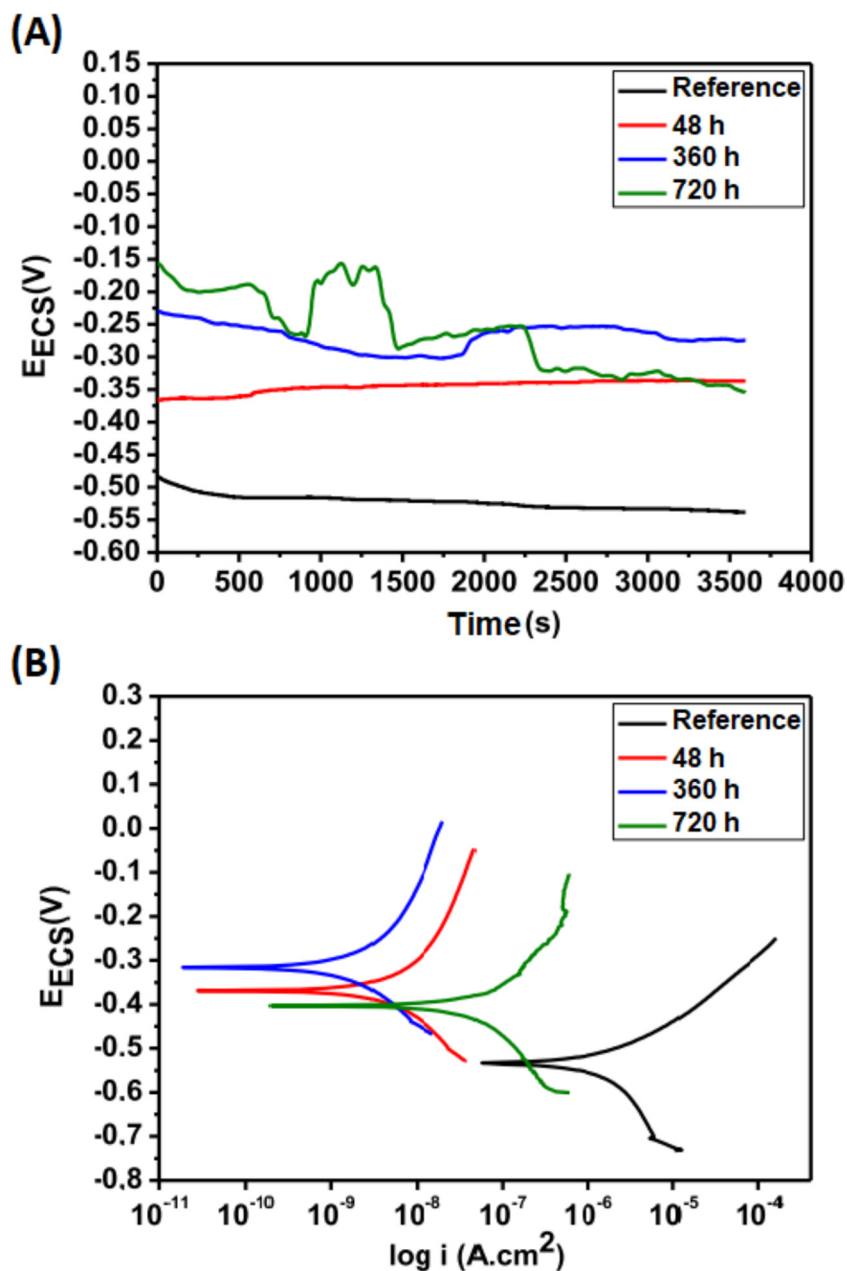
Fig. 7. N80 steel electrochemical features after different exposure times along wet carbonation experiments: (A) open-circuit potential and (B) potentiodynamic polarization curves.

Table 4
Electrochemical results of the N80 steel cores.

Parameters	Time			
	0 h	48 h	360 h	720 h
Ecorr (mV)	−535	−369	−316	−404
icorr (μA/cm^2)	9.360	0.028	0.010	0.319
[1]PR (Ωcm^2)	2.8×10^3	9.3×10^5	2.6×10^6	8.2×10^4
[2]CR (mm/year)	0.1081	0.0003	0.0001	0.0037

[1] PR - polarization resistance.

[2] CR - corrosion rate.

future works with a greater number of experiments and longer degradation times.

3.2.4. SEM-EDS line scan analysis

Fig. 8 shows SEM-EDS line scan analyses for cement (Fig. 8A) and steel (Fig. 8B) phases from the unaltered zone to the degraded interfacial zone. In the present work, these analyses were useful to confirm the previous statements about the material exchange flow in the cement-casing carbonation process so giving support to the discussion about wellbore material degradation process dynamics in the presence of interfacial defects.

In the cement SEM-EDS line scan (Fig. 8A), point number one (1) corresponds to the beginning of the carbonated zone, point number two (2) corresponds to the beginning of the bicarbonated zone and point number three (3) is the periphery of the cement paste core in the cement-casing interfacial region. Before the carbonated zone, we observe that there is a Ca content decrease and a Si content increase in relation
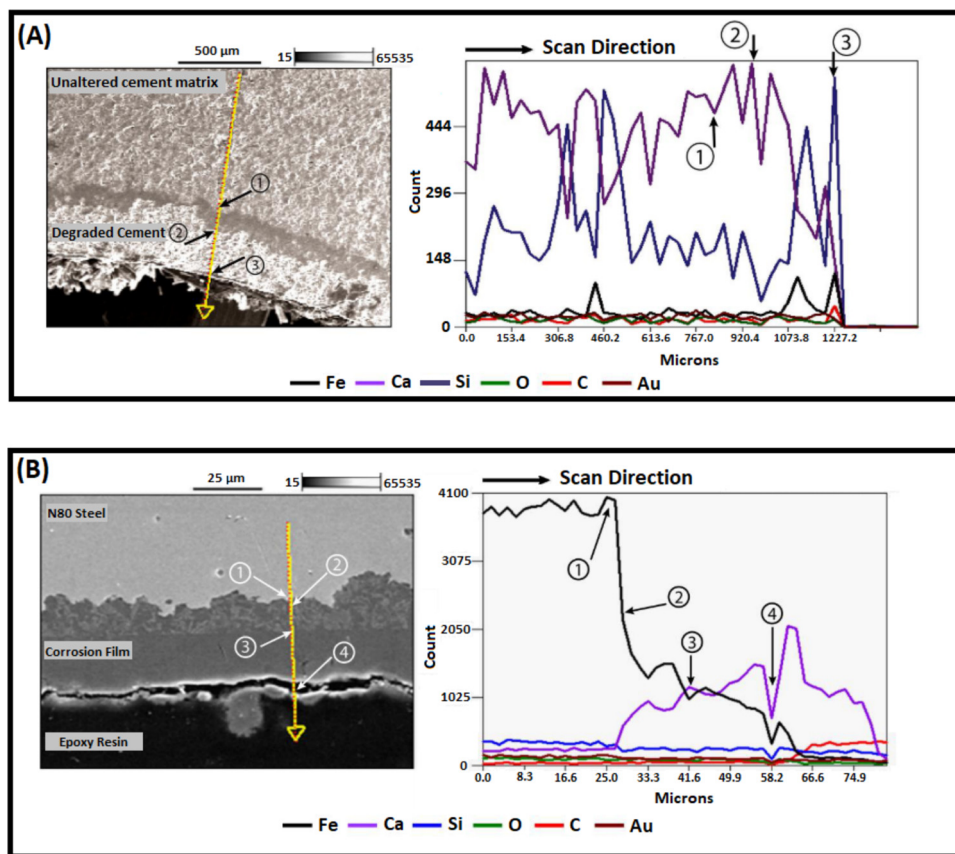
Fig. 8. SEM-EDS line scan analysis of the cement-casing interfaces after exposure to CO_2-rich brine: (A) cement phase and (B) steel phase.

to the unaltered cement paste, indicating portlandite dissolution and relative enrichment of the C-S-H phase (Koukouzas et al., 2017). From point one (1) to point two (2), the Ca content shows a tendency to increase due to the carbonation process. Since $CaCO_3$ partially fills the porosity of the cement paste, the relative calcium (Ca) concentration of the carbonate zone increases (Tiong et al., 2019). However, as scanning advances through the bicarbonated zone to the interfacial defect region (from point 2–3), the Ca content reduces, and Si content increases due to the bicarbonation process involving the carbonate dissolution and formation of amorphous silica. In addition, the Fe content increases near the interfacial defect region indicating Fe ions migration from the corroded steel surface to the cement matrix, being subsequently fixed by precipitation in carbonate form (Tremosa et al., 2017; Wolterbeek et al., 2013).

On the steel SEM-EDS line scan (Fig. 8B) point one (1) corresponds to the non-corroded steel in the vicinity of the film's inner layer; point two (2) to the beginning of the corrosion product's inner layer; point three (3) to the beginning of the corrosion product's outer layer; and point four (4) to the region between the outer layer of the corrosion product film and the epoxy resin employed for the metallographic inlay. From EDS elemental results, it can be observed that in point one (1) the steel matrix is perfectly preserved and presents the highest Fe count. From point one (1) to point two (2), the Fe profile shows a decreasing tendency along the corrosion film. In this zone, the Ca content is still low, but its concentration is not negligible meaning that the fluids are able to percolate through the corrosion film. The region from point two (2) to point three (3) represents the transition between the inner and outer corrosion layer, showing an inversion in the Fe and Ca concentrations. This means that the mixed carbonate ($Fe_xCa_yCO_3$) changes its profile from Fe-rich carbonate to Ca-rich carbonate during the degradation process. This behavior continues until the outer layer boundary (point 4) meaning that Ca leached from the cement matrix

can migrate to the steel surface and precipitate as calcium carbonate ($CaCO_3$) and mixed Fe-Ca carbonate ($Fe_xCa_yCO_3$).

This data corroborates with results previously presented by Wolterbeek and co-authors (2013) showing that steel corrosion in a CO_2-rich medium is influenced by the cement sheath, resulting in the formation of corrosion products with different protective features. These corrosion layers present a broad composition ranging from iron carbonate ($FeCO_3$), passing through different compositions of mixed carbonates ($Fe_xCa_yCO_3$) and finally forming calcium carbonate ($CaCO_3$) at the material boundary. As the Ca and Fe availability in the medium changes when mineral saturation is reached, Fe^{2+} ions are replaced by Ca^{2+} ions resulting in the formation of mixed carbonates. Unlike iron carbonate ($FeCO_3$), mixed ($Fe_xCa_yCO_3$) and calcium ($CaCO_3$) carbonates present a low protective capacity and, as the protective film undergoes dissolution/reprecipitation processes, it allows the corrosion front to advance through the steel surface (Esmaeely et al., 2013; Navabzadeh Esmaeely et al., 2013). Thus, as the protective film changes its profile, the medium loses its ability to prevent corrosion and depending on the local dynamics, it can result in the formation of localized corrosion (pitting corrosion) possibly compromising the integrity of the casing.

In addition to calcium effects on the corrosion film, we may observe the consequences of the iron migration into the cement matrix as well. It is detailed in the literature that iron may inhibit the calcite ($CaCO_3$) formation along the carbonation process, and thus favors the formation of other $CaCO_3$ polymorphs such as aragonite and vaterite (Alsaiari et al., 2008; Wolterbeek et al., 2013). Among the disadvantages of calcite formation inhibition are: (i) reduction in the cement self-healing capacity and (ii) reduction in the pore block efficiency of the cement carbonation products. Both disadvantages reduce the cement potential to withstand the intrusion of acidic fluids into its matrix resulting in a quicker loss of wellbore integrity. Based on Figs. 6, S11 (Supplementary
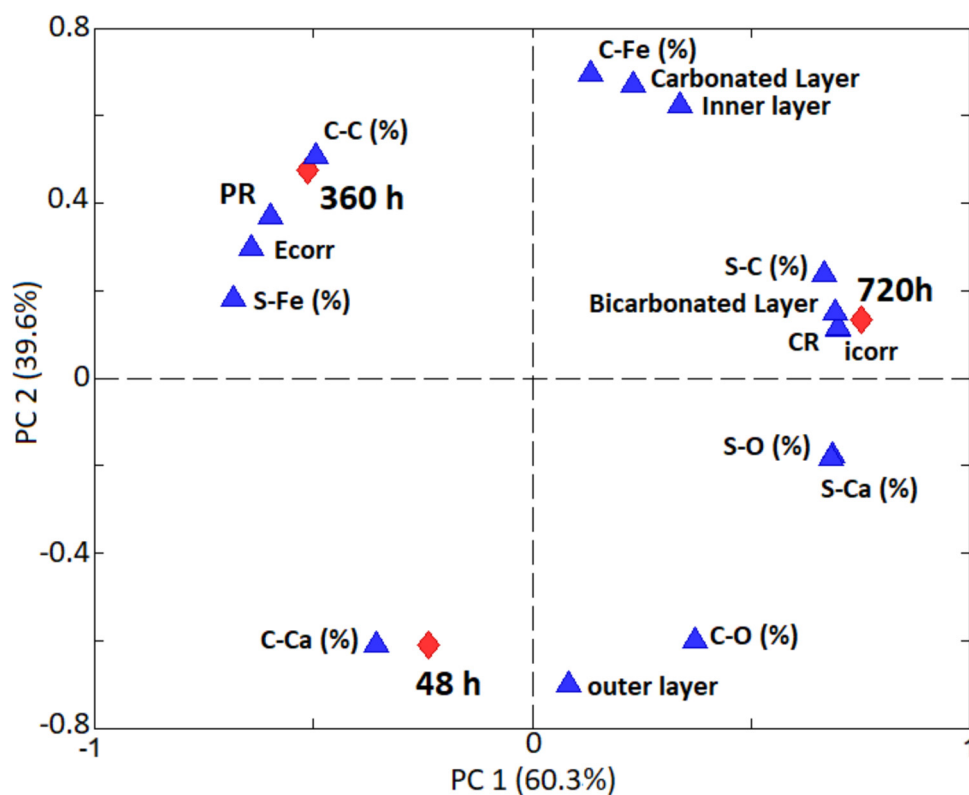
Fig. 9. Principal component analysis of degradation, elemental and electrochemical results of the cement-casing interfacial system.

Material) and EDS analysis, only the presence of aragonite and vaterite $CaCO_3$ polymorphs and mixed carbonates $(Fe_xCa_yCO_3)$ can be observed. However, the identity of the $CaCO_3$ polymorphs and other minerals must be evaluated in future works using more accurate methods, such as X-ray diffraction analysis.

3.2.5. Data analysis

In the present work, data analysis was performed using correlation analysis (Fig. S10 and Table S3 on the Supplementary Material) and the PCA (Fig. 9) applying the degraded layer data (Table 2), the EDS elemental profile (Table 3) and the electrochemical data (Table 4) of specimens exposed to CO_2-rich brine degradation (48 h, 360 h and 720 h). For brevity, only the most important correlations are discussed in the present work, however, numerical linear relationship results among the parameters are detailed in Table S3 in the Supplementary Material.

From the PCA results, only two principal components (PC 1–60.3 % and PC 2–39.6 %) represent 99.9 % of the data set explained variance. In addition, according to the PCA biplot we may correlate the 48 h specimens with higher values of calcium fraction in the cement (C-Ca) and a thicker outer corrosion layer, while the 360 h specimens correlate with a higher iron fraction in the steel (S-Fe), greater corrosion potential (Ecorr) and elevated polarization resistance (PR), and the 720 h specimens correlate with a higher corrosion rate (CR), greater iron fraction in the cement (C-Fe) and thicker carbonated (CL), bicarbonated (BL) and inner corrosion layers.

In conjunction with the correlation analysis (Fig. S10 and Table S3), these features indicate that at short exposure times (48 h), part of the Ca precipitates in the cement matrix, increasing its relative fraction on the cement surface while, at the same time, the Ca from the portlandite dissolution migrates to the steel surface composing the outer corrosion layer. At intermediate exposure times (360 h), the lowest corrosion rate (0.0001 mm/year) could be explained by the formation of a protective iron carbonate ($FeCO_3$) layer, mostly composing the inner corrosion layer. For longer exposure times (720 h), higher corrosion rates are

correlated to an increase in the protective (inner) and non-protective (outer) corrosion layers, which means that the combination of the corrosion products confers less protection against the advance of the corrosion front. In addition, from the positive correlation between the iron fraction in the cement (C-Fe) with the inner corrosion layer thickness ($R^2 = 0.95$, according to Table S3), we may state that iron ions (Fe) in the cement matrix come from the inner layer dissolution as the degradation front advances.

3.2.6. Dynamic flux through the cement, steel and CO_2-rich brine phases

Up to date, there is significant lack of data about cement-casing degradation dynamics in the presence of wellbore interfacial defects. Results previously discussed were based on significantly small interfacial gap spacings (µm) (Wolterbeek et al., 2013) and, from the present work, we have identified that a similar profile was observed for much larger gap spacings (approx. 1.5 mm). Some defects may result in similar spacings between the cement and casing including: (i) drilling or operational damage to the cement sheath, (ii) wellbore completion failures, (iii) void spaces, (iv) severe fractures and (v) mud or gas channels. These defects are the same that makes CO_2-rich fluids migrate through the cement matrix, possibly reaching shallower wellbore sections.

Thus, based on the present work and data previously obtained from the literature, Fig. 10 revises the processes and dynamics of the cement-casing degradation in the presence of CO_2-rich brine in an interfacial defect. The EDS line scan data (Fig. 8A and B) supports the assumption that the formation order of the degraded products on the material surface is: (i) $CaCO_3 \rightarrow Fe_xCa_yCO_3 \rightarrow$ and $FeCO_3$ for the cement, and (ii) $FeCO_3 \rightarrow Fe_xCa_yCO_3 \rightarrow CaCO_3$ for the steel.

From Fig. 10, the wet degradation process starts with CO_2 dissolution in brine forming carbonate (CO_3^{2-}) and bicarbonate (HCO3-) ions. As these ions diffuse through the interfacial defect and reach the materials surface (cement and steel), the degradation process begins. In the first moment, the CO_2-rich brine affects the steel surface more intensively, resulting in casing corrosion, leaching Fe^{2+} ions into solution
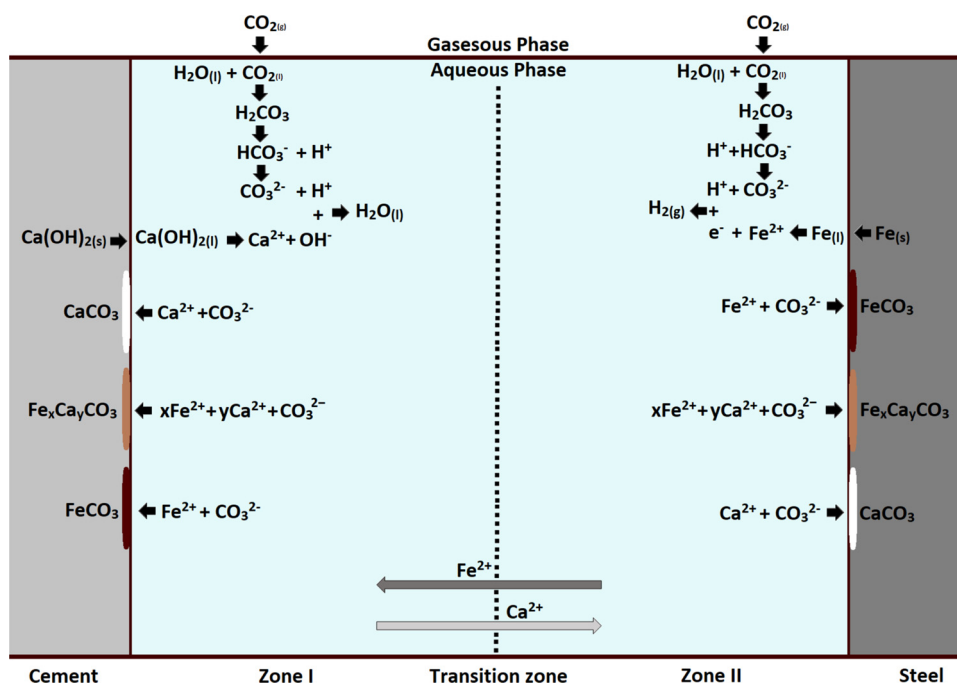
Fig. 10. Dynamics and material exchange flows in the cement-casing-CO_2-rich brine system. Chemical reaction in the cement-casing system over the cement layer (Zone I) and on the N80 corrosion (Zone II).

and inducing the $FeCO_3$ precipitation on the steel surface. This corrosion layer presents protective features and can delay further advances of the corrosion front. Otherwise, on the cement surface two processes are occurring: (i) the dissolution of portlandite in the solution, increasing the pH and Ca concentration in the medium and (ii) the carbonation process of the cement, forming calcium carbonate ($CaCO_3$) and thus reducing the material porosity.

Then, as the degradation process progresses, the flow of calcium ions from the cement matrix (Zone I) to near the steel (Zone II), and the flow of iron ions from the steel casing (Zone II) to near the cement (Zone I), becomes significant. At a given moment, Fe starts to migrate into the cement structure compromising the material's self-healing and pore-blocking, and Ca begins to compose the corrosion film from the formation of mixed carbonates ($Fe_xCa_yCO_3$), thus compromising the corrosion layer protection efficiency. Finally, both ions (Ca^{2+} and Fe^{2+}) become so abundant in the material vicinity that it is possible to form calcium carbonates ($CaCO_3$) on the corrosion layer and iron carbonate ($FeCO_3$) precipitates in the cement matrix. At this point, the system may completely lose its ability to withstand further advances of the degradation process.

4. Conclusions

From the experiments showing no interfacial defect, no signs of degradation or fluid intrusion were observed along the cement-casing interface, meaning that a perfectly bonded cement can efficiently protect the steel casing against CO_2 degradation, acting as a barrier to prevent CO_2 leakage from the CCS storage formation. Already, from the experiments showing interfacial defect, both cement and steel undergo significant degradation processes. From our results we found that CO_2-rich brine first affects the steel surface, resulting in the leaching of Fe^{2+} ions into solution and inducing the $FeCO_3$ precipitation on the steel surface. This corrosion layer presents protective features and can delay further advances of the corrosion front. Otherwise, two processes occur on the cement surface: (i) the dissolution of portlandite increasing the pH and the calcium (Ca) concentration in the medium, and (ii) the cement carbonation process resulting in the formation of calcium carbonate ($CaCO_3$), thus reducing the material porosity.

As the degradation process evolves, the iron (Fe) ions starts to migrate into the cement structure, compromising the material self-healing and pore-blocking features, while the calcium (Ca) ions begin to compose the corrosion film from the formation of mixed carbonates ($Fe_xCa_yCO_3$), compromising the corrosion layer protection efficiency. Finally, both ions (Ca^{2+} and Fe^{2+}) become so abundant in the material's vicinity that they may form calcium carbonates ($CaCO_3$) on the corrosion layer and precipitate iron carbonate ($FeCO_3$) in the cement matrix. At this point, the system may completely lose its ability to withstand further advances of the degradation process.

From our work, significant advances are obtained on the study of the degradation of cement-casing systems showing interfacial defect in a quasi-static medium under CO_2-rich environments. In addition, we may conclude that the formation-cement-casing system should be jointly studied, since significant interactive parameters were identified. However, future works should simulate the influence of other parameters that can alter the dynamics of the CO_2 degradation process of the cement-casing system with interfacial defects such as: (i) the cement hydration time, (ii) the influence of the casing steel alloy type, (iii) the presence of other fluids like mud and spacer in the voids, instead of brine, (iv) evaluate the process under different conditions of temperature, pressure and time, and (v) study the degradation process considering the existence of a dynamic fluid flow between the cement-casing interface (simulating a leak of CO_2).

CRediT authorship contribution statement

Felipe Dalla Vecchia: Conceptualization, Methodology, Software, Validation, Formal analysis, Investigation, Resources, Data curation, Writing - original draft, Writing - review & editing, Visualization, Supervision, Project administration, Funding acquisition. **Victor Hugo Jacks Mendes dos Santos:** Software, Validation, Formal analysis, Investigation, Data curation, Writing - original draft, Writing - review & editing, Visualization. **Marta Kerber Schütz:** Validation, Formal analysis, Investigation, Data curation, Writing - original draft, Writing - review & editing, Visualization. **Gabriela Gonçalves Dias Ponzi:** Methodology, Validation, Formal analysis. **Amanda Sofia de Guimarães e Stepanha:** Methodology, Validation, Formal analysis.

Célia de Fraga Malfatti: Methodology, Validation, Formal analysis, Visualization. **Eleani Maria da Costa:** Conceptualization, Investigation, Resources, Data curation, Supervision, Project administration, Funding acquisition.

Declaration of Competing Interest

None.

Acknowledgments

Appendix A. Supplementary data

Supplementary material related to this article can be found, in the online version, at doi:https://doi.org/10.1016/j.ijggc.2020.103077.

References

Ahdaya, M.S., Imqam, A., Jani, P., Fakher, S., ElGawady, M., 2019. New formulation of fly ash class C based geopolymer for oil Well cementing. In: International Petroleum Technology Conference. International Petroleum Technology Conference. https://doi.org/10.2523/19393-MS.

Ajayi, T., Gupta, I., 2019. A review of reactive transport modeling in wellbore integrity problems. J. Pet. Sci. Eng. 175, 785–803. https://doi.org/10.1016/j.petrol.2018.12.079.

Alsaiari, H.A., Yean, S., Tomson, M.B., Kan, A.T., 2008. Iron calcium carbonate: precipitation interaction, in: SPE international oilfield scale conference. Old Spe J. 28–29. https://doi.org/10.2118/114064-MS.

American Petroleum Institute, A., 2002. API 10A. Specification for cements and materials for well cementing. Am. Pet. Inst. Publ. Serv. Washingt. DC.

Asahara, Y., Mito, S., Xue, Z., Yamashita, Y., Miyashiro, K., 2013. Chemical impacts of CO_2 flooding on well composite samples: experimental assessment of well integrity for CO_2 sequestration. Energy Procedia 37, 5738–5745. https://doi.org/10.1016/j.egypro.2013.06.496.

ASTM International, 2019. ASTM G3-14: Standard Practice for Conventions Applicable to Electrochemical Measurements. ASTM Stand, West Conshohocken, pp. 1–9. https://doi.org/10.1520/G0003-89R10.2.

Bagheri, M., Shariatipour, S.M., Ganjian, E., 2018. A review of oil well cement alteration in CO_2-rich environments. Constr. Build. Mater. 186, 946–968. https://doi.org/10.1016/j.conbuildmat.2018.07.250.

Bai, M., Sun, J., Song, K., Li, L., Qiao, Z., 2015a. Well completion and integrity evaluation for CO_2 injection wells. Renewable Sustainable Energy Rev. 45, 556–564. https://doi.org/10.1016/j.rser.2015.02.022.

Bai, M., Sun, J., Song, K., Reinicke, K.M., Teodoriu, C., 2015b. Evaluation of mechanical well integrity during CO_2 underground storage. Environ. Earth Sci. 73, 6815–6825. https://doi.org/10.1007/s12665-015-4157-5.

Barlet-Gouédard, V., Rimmelé, G., Goffé, B., Porcherie, O., 2007. Well technologies for CO_2 geological storage: CO_2-resistant cement. Oil Gas Sci. Technol. - Rev. l'IFP 62, 325–334. https://doi.org/10.2516/ogst:2007027.

Barlet-Gouédard, V., Rimmelé, G., Porcherie, O., Quisel, N., Desroches, J., 2009. A solution against well cement degradation under CO_2 geological storage environment. Int. J. Greenh. Gas Control 3, 206–216. https://doi.org/10.1016/j.ijggc.2008.07.005.

Beck, J., Feng, R., Hall, D.M., Buyuksagis, A., Ziomek-Moroz, M., Lvov, S.N., 2016. Effects of H_2S and CO_2 on cement/casing interface corrosion integrity for cold climate oil and gas well applications. ECS Trans. 72, 107–122. https://doi.org/10.1149/07217.0107ecst.

Bihua, X., Bin, Y., Yongqing, W., 2018. Anti-corrosion cement for sour gas (H_2S-CO_2) storage and production of HTHP deep wells. Appl. Geochem. 96, 155–163. https://doi.org/10.1016/j.apgeochem.2018.07.004.

Bjørge, R., Gawel, K., Chavez Panduro, E.A., Torsæter, M., 2019. Carbonation of silica cement at high-temperature well conditions. Int. J. Greenh. Gas Control 82, 261–268. https://doi.org/10.1016/j.ijggc.2019.01.011.

Carey, J.W., Wigand, M., Chipera, S.J., WoldeGabriel, G., Pawar, R., Lichtner, P.C., Wehner, S.C., Raines, M.A., Guthrie, G.D., 2007. Analysis and performance of oil well cement with 30 years of CO_2 exposure from the SACROC Unit, West Texas, USA. Int. J. Greenh. Gas Control 1, 75–85. https://doi.org/10.1016/S1750-5836(06)00004-1.

Carey, J.W., Svec, R., Grigg, R., Lichtner, P.C., Zhang, J., Crow, W., 2009. Wellbore integrity and CO_2-brine flow along the casing-cement microannulus. Energy Procedia 1, 3609–3615. https://doi.org/10.1016/j.egypro.2009.02.156.

Carey, J.W., Svec, R., Grigg, R., Zhang, J., Crow, W., 2010. Experimental investigation of wellbore integrity and CO_2–brine flow along the casing–cement microannulus. Int. J. Greenh. Gas Control 4, 272–282. https://doi.org/10.1016/j.ijggc.2009.09.018.

Carroll, S., Carey, J.W., Dzombak, D., Huerta, N.J., Li, L., Richard, T., Um, W., Walsh, S.D.C., Zhang, L., 2016. Review: role of chemistry, mechanics, and transport on well integrity in CO_2 storage environments. Int. J. Greenh. Gas Control 49, 149–160. https://doi.org/10.1016/j.ijggc.2016.01.010.

Celia, M.A., Bachu, S., Nordbotten, J.M., Bandilla, K.W., 2015. Status of CO_2 storage in deep saline aquifers with emphasis on modeling approaches and practical simulations. Water Resour. Res. 51, 6846–6892. https://doi.org/10.1002/2015WR017609.

Choi, Y., Young, D., Nešić, S., Gray, L.G.S., 2013. Wellbore integrity and corrosion of carbon steel in CO_2 geologic storage environments: a literature review. Int. J. Greenh. Gas Control 16, S70–S77. https://doi.org/10.1016/j.ijggc.2012.12.028.

Crow, W., Carey, J.W., Gasda, S., Brian Williams, D., Celia, M., 2010. Wellbore integrity analysis of a natural CO_2 producer. Int. J. Greenh. Gas Control 4, 186–197. https://doi.org/10.1016/j.ijggc.2009.10.010.

Ding, C., Gao, Kwei, Chen, Cfeng, 2009. Effect of Ca^{2+} on CO_2 corrosion properties of X65 pipeline steel. Int. J. Miner. Metall. Mater. 16, 661–666. https://doi.org/10.1016/S1674-4799(10)60009-X.

Duguid, A., Scherer, G.W., 2010. Degradation of oilwell cement due to exposure to carbonated brine. Int. J. Greenh. Gas Control 4, 546–560. https://doi.org/10.1016/j.ijggc.2009.11.001.

Duguid, A., Radonjic, M., Scherer, G.W., 2011. Degradation of cement at the reservoir/cement interface from exposure to carbonated brine. Int. J. Greenh. Gas Control 5, 1413–1428. https://doi.org/10.1016/j.ijggc.2011.06.007.

Duguid, A., Carey, J.W., Butsch, R., 2014. Well integrity assessment of a 68 year old well at a CO_2 injection project. Energy Procedia 63, 5691–5706. https://doi.org/10.1016/j.egypro.2014.11.602.

Duguid, A., Guo, B., Nygaard, R., 2017. Well integrity assessment of monitoring wells at an active CO_2-EOR flood. Energy Procedia 114, 5118–5138. https://doi.org/10.1016/j.egypro.2017.03.1667.

Esmaeely, S.N., Choi, Y., Young, D., Nesic, S., Technology, M., 2013. Effect of calcium on the formation and protectiveness of iron carbonate layer in CO_2 corrosion. NACE - International Corrosion Conference Series 1–13.

Garcia Fernandez, S., Matteo, E.N., Taha, M.R., Stormont, J.C., 2019. Characterization of wellbore microannuli. J. Nat. Gas Sci. Eng. 62, 13–25. https://doi.org/10.1016/j.jngse.2018.12.003.

Gawel, K., Todorovic, J., Liebscher, A., Wiese, B., Opedal, N., 2017. Study of materials retrieved from a ketzin CO_2 monitoring well. Energy Procedia 114, 5799–5815. https://doi.org/10.1016/j.egypro.2017.03.1718.

Guthrie, G.D., Pawar, R.J., Carey, J.W., Karra, S., Harp, D.R., Viswanathan, H.S., 2018. The mechanisms, dynamics, and implications of self-sealing and CO_2 resistance in wellbore cements. Int. J. Greenh. Gas Control 75, 162–179. https://doi.org/10.1016/j.ijggc.2018.04.006.

Hawkes, C.D., Gardner, C., 2013. Pressure transient testing for assessment of wellbore integrity in the IEAGHG Weyburn–Midale CO_2 Monitoring and Storage Project. Int. J. Greenh. Gas Control 16, S50–S61. https://doi.org/10.1016/j.ijggc.2012.12.022.

Iglesias, R.S., Ketzer, J.M., Melo, C.L., Heemann, R., Machado, C.X., 2015. Carbon capture and geological storage in Brazil: an overview. Greenh. Gases Sci. Technol. 5, 119–130. https://doi.org/10.1002/ghg.1476.

International, A.S.T.M., 2015. ASTM G102-89: Standard Practice for Calculation of Corrosion Rates and Related Information From Electrochemical Measurements. ASTM Stand, West Conshohocken, pp. 1–7. https://doi.org/10.1520/G0102-89R15E01.2.

Iyer, J., Walsh, S.D.C., Hao, Y., Carroll, S.A., 2018. Assessment of two-phase flow on the chemical alteration and sealing of leakage pathways in cemented wellbores. Int. J. Greenh. Gas Control 69, 72–80. https://doi.org/10.1016/j.ijggc.2017.12.001.

Jobard, E., Sterpenich, J., Pironon, J., Corvisier, J., Randi, A., 2018. Experimental modelling of the Caprock/cement interface behaviour under CO_2 storage conditions: effect of water and supercritical CO_2 from a cathodoluminescence study. Geosciences 8, 185. https://doi.org/10.3390/geosciences8050185.

Ketzer, J.M., Iglesias, R., Einloft, S., Dullius, J., Ligabue, R., de Lima, V., 2009. Water-rock-CO_2 interactions in saline aquifers aimed for carbon dioxide storage: experimental and numerical modeling studies of the Rio Bonito Formation (Permian), southern Brazil. Appl. Geochem. 24, 760–767. https://doi.org/10.1016/j.apgeochem.2009.01.001.

Kiran, R., Teodoriu, C., Dadmohammadi, Y., Nygaard, R., Wood, D., Mokhtari, M., Salehi, S., 2017. Identification and evaluation of well integrity and causes of failure of well integrity barriers (A review). J. Nat. Gas Sci. Eng. 45, 511–526. https://doi.org/10.1016/j.jngse.2017.05.009.

Koukouzas, N., Kypritidou, Z., Vasilatos, C., Tsoukalas, N., Rochelle, C.A., Purser, G., 2017. Geochemical modeling of carbonation of hydrated oil well cement exposed to CO_2-saturated brine solution. Appl. Geochem. 85, 35–48. https://doi.org/10.1016/j.apgeochem.2017.08.002.

Laumb, J.D., Glazewski, K.A., Hamling, J.A., Azenkeng, A., Watson, T.L., 2016. Wellbore corrosion and failure assessment for CO_2 EOR and storage: two case studies in the Weyburn field. Int. J. Greenh. Gas Control 54, 479–489. https://doi.org/10.1016/j.ijggc.2016.08.031.

Lavrov, A., 2018. Stiff cement, soft cement: nonlinearity, arching effect, hysteresis, and irreversibility in CO_2-well integrity and near-well geomechanics. Int. J. Greenh. Gas Control 70, 236–242. https://doi.org/10.1016/j.ijggc.2017.11.012.

Lavrov, A., Torsæter, M., 2018. All microannuli are not created equal: role of uncertainty and stochastic properties in well leakage prediction. Int. J. Greenh. Gas Control 79, 323–328. https://doi.org/10.1016/j.ijggc.2018.09.001.

Lesti, M., Tiemeyer, C., Plank, J., 2013. CO_2 stability of Portland cement based well cementing systems for use on carbon capture & storage (CCS) wells. Cem. Concr. Res.

45, 45–54. https://doi.org/10.1016/j.cemconres.2012.12.001.

Li, Y., Nygaard, R., 2018. A numerical study on the feasibility of evaluating CO_2 injection wellbore integrity through casing deformation monitoring. Greenh. Gases Sci. Technol. 8, 51–62. https://doi.org/10.1002/ghg.1733.

Lorek, A., Labus, M., Bujok, P., 2016. Wellbore cement degradation in contact zone with formation rock. Environ. Earth Sci. 75, 499. https://doi.org/10.1007/s12665-015-5114-z.

Machado, C.X., Rockett, G.C., Ketzer, J.M.M., 2013. Brazilian renewable carbon capture and geological storage map: possibilities for the Paraná basin. Energy Procedia 37, 6105–6111. https://doi.org/10.1016/j.egypro.2013.06.539.

Manceau, J.C.C., Tremosa, J., Lerouge, C., Gherardi, F., Nussbaum, C., Wasch, L.J.J., Alberic, P., Audigane, P., Claret, F., 2016. Well integrity assessment by a 1:1 scale wellbore experiment: exposition to dissolved CO_2 and overcoring. Int. J. Greenh. Gas Control 54, 258–271. https://doi.org/10.1016/j.ijggc.2016.09.012.

Metz, B., Davidson, O., De Coninck, H., 2005. Carbon Dioxide Capture and Storage: Special Report of the Intergovernmental Panel on Climate Change. Cambridge University Press, Intergovernmental Panel on Climate Change. Intergovernmental Panel on Climate Change, Geneva (Switzerland).

Mito, S., Xue, Z., Satoh, H., 2015. Experimental assessment of well integrity for CO_2 geological storage: batch experimental results on geochemical interactions between a CO_2–brine mixture and a sandstone–cement–steel sample. Int. J. Greenh. Gas Control 39, 420–431. https://doi.org/10.1016/j.ijggc.2015.06.007.

Nakano, K., Ohbuchi, A., Mito, S., Xue, Z., 2014. Chemical Interaction of well composite samples with supercritical CO_2 along the cement - sandstone interface. Energy Procedia 63, 5754–5761. https://doi.org/10.1016/j.egypro.2014.11.608.

Nakano, K., Mito, S., Xue, Z., Ohbuchi, A., 2016. Observation of Cement/Sandstone interface after reaction with supercritical CO_2 using SEM-EDS, μ-XRD, and μ-Raman spectroscopy. E-J. Surf. Sci. Nanotechnol. 14, 198–203. https://doi.org/10.1380/ejssnt.2016.198.

Navabzadeh Esmaeely, S., Choi, Y.-S., Young, D., Nešić, S., 2013. Effect of calcium on the formation and protectiveness of iron carbonate layer in CO_2 corrosion. CORROSION 69, 912–920. https://doi.org/10.5006/0942.

Nešić, S., 2007. Key issues related to modelling of internal corrosion of oil and gas pipelines – a review. Corros. Sci. 49, 4308–4338. https://doi.org/10.1016/j.corsci.2007.06.006.

Omosebi, O., Maheshwari, H., Ahmed, R., Shah, S., Osisanya, S., Hassani, S., DeBruijn, G., Cornell, W., Simon, D., 2016. Degradation of well cement in HPHT acidic environment: effects of CO_2 concentration and pressure. Cem. Concr. Compos. 74, 54–70. https://doi.org/10.1016/j.cemconcomp.2016.09.006.

Omosebi, O.A., Sharma, M., Ahmed, R.M., Shah, S.N., Saasen, A., Osisanya, S.O., 2017. Cement degradation in CO_2 - H_2S environment under high pressure-high temperature conditions. In: SPE Bergen One Day Seminar. Society of Petroleum Engineers. https://doi.org/10.2118/185932-MS.

Onishi, T., Nguyen, M.C., Carey, J.W., Will, B., Zaluski, W., Bowen, D.W., Devault, B.C., Duguid, A., Zhou, Q., Fairweather, S.H., Spangler, L.H., Stauffer, P.H., 2019. Potential CO_2 and brine leakage through wellbore pathways for geologic CO_2 sequestration using the national risk assessment partnership tools: application to the big sky regional partnership. Int. J. Greenh. Gas Control 81, 44–65. https://doi.org/10.1016/j.ijggc.2018.12.002.

Pfennig, A., Kranzmann, A., 2018. Impact of saline aquifer water on surface and shallow pit corrosion of martensitic stainless steels during exposure to CO_2 environment (CCS). IOP Conf. Ser. Earth Environ. Sci. 150, 012012. https://doi.org/10.1088/1755-1315/150/1/012012.

Pfennig, A., Zastrow, P., Kranzmann, A., 2013. Supercritical CO_2-corrosion in heat treated

steel pipes during carbon capture and storage CCS. Springer Series in Geomechanics and Geoengineering 39–51. https://doi.org/10.1007/978-3-642-37849-2_4.

Pfennig, A., Wolthusen, H., Kranzmann, A., 2017. Unusual corrosion behavior of 1.4542 exposed a laboratory saline aquifer water CCS-environment. Energy Procedia 114, 5229–5240. https://doi.org/10.1016/j.egypro.2017.03.1679.

Postma, T.J.W., Bandilla, K.W., Celia, M.A., 2019. Estimates of CO_2 leakage along abandoned wells constrained by new data. Int. J. Greenh. Gas Control 84, 164–179. https://doi.org/10.1016/j.ijggc.2019.03.022.

Ren, C., Peng, Y., Li, B., Wang, S., Shi, T., 2016. Interfacial evolution of cement and steel in CO_2 dissolved solution under high temperature and high pressure. High Temp. Mater. Process. 35, 821–826. https://doi.org/10.1515/htmp-2015-0125.

Rocha, W.F.C., Vaz, B.G., Sarmanho, G.F., Leal, L.H.C., Nogueira, R., Silva, V.F., Borges, C.N., 2012. Chemometric techniques applied for classification and quantification of binary biodiesel/diesel blends. Anal. Lett. 45, 2398–2411. https://doi.org/10.1080/00032719.2012.686135.

Rockett, G.C., Machado, C.X., Ketzer, J.M.M., Centeno, C.I., 2011. The CARBMAP project: Matching CO_2 sources and geological sinks in Brazil using geographic information system. Energy Procedia 4, 2764–2771. https://doi.org/10.1016/j.egypro.2011.02.179.

Silva, J.C., Milestone, N.B., 2018a. Cement/rock interaction in geothermal wells. The effect of silica addition to the cement and the impact of CO_2 enriched brine. Geothermics 73, 16–31. https://doi.org/10.1016/j.geothermics.2018.01.004.

Silva, J.C., Milestone, N.B., 2018b. The effect of the rock type on the degradation of well cements in CO_2 enriched geothermal environments. Geothermics 75, 235–248. https://doi.org/10.1016/j.geothermics.2018.06.002.

Teodoriu, C., Bello, O., 2020. A review of cement testing apparatus and methods under CO_2 environment and their impact on well integrity prediction – where do we stand? J. Pet. Sci. Eng. 187, 106736. https://doi.org/10.1016/j.petrol.2019.106736.

Tiong, M., Gholami, R., Rahman, M.E., 2019. Cement degradation in CO_2 storage sites: a review on potential applications of nanomaterials. J. Pet. Explor. Prod. Technol. 9, 329–340. https://doi.org/10.1007/s13202-018-0490-z.

Tremosa, J., Mito, S., Audigane, P., Xue, Z., 2017. Experimental assessment of well integrity for CO_2 geological storage: a numerical study of the geochemical interactions between a CO_2-brine mixture and a sandstone-cement-steel sample. Appl. Geochem. 78, 61–73. https://doi.org/10.1016/j.apgeochem.2016.12.011.

Vasanthavigar, M., Srinivasamoorthy, K., Prasanna, M.V., 2013. Identification of groundwater contamination zones and its sources by using multivariate statistical approach in Thirumanimuthar sub-basin, Tamil Nadu, India. Environ. Earth Sci. 68, 1783–1795. https://doi.org/10.1007/s12665-012-1868-8.

Wakeel, S.Al, Němeček, J., Li, L., Xi, Y., Hubler, M., 2019. The effect of introducing nanoparticles on the fracture toughness of well cement paste. Int. J. Greenh. Gas Control 84, 147–153. https://doi.org/10.1016/j.ijggc.2019.03.009.

Wolterbeek, T.K.T., Raoof, A., 2018. Meter-scale reactive transport modeling of CO_2-rich fluid flow along debonded wellbore casing-cement interfaces. Environ. Sci. Technol. 52, 3786–3795. https://doi.org/10.1021/acs.est.7b05358.

Wolterbeek, T.K.T., Peach, C.J., Spiers, C.J., 2013. Reaction and transport in wellbore interfaces under CO_2 storage conditions: experiments simulating debonded cement–casing interfaces. Int. J. Greenh. Gas Control 19, 519–529. https://doi.org/10.1016/j.ijggc.2013.10.017.

Wolterbeek, T.K.T., Peach, C.J., Raoof, A., Spiers, C.J., 2016. Reactive transport of CO_2-rich fluids in simulated wellbore interfaces: flow-through experiments on the 1–6 m length scale. Int. J. Greenh. Gas Control 54, 96–116. https://doi.org/10.1016/j.ijggc.2016.08.034.